

Constraining intermediate-mass black holes from the stellar disc of SgrA*

Jean-Baptiste Fouvy¹, María José Bustamante-Rosell², Aaron Zimmerman³

¹ CNRS and Sorbonne Université, UMR 7095, Institut d’Astrophysique de Paris, 98 bis Boulevard Arago, F-75014 Paris, France

² Department of Astronomy and Astrophysics, University of California, Santa Cruz, CA 95064, USA

³ Weinberg Institute, University of Texas at Austin, Austin, TX 78712, USA

26 May 2023

ABSTRACT

Stars evolving around a supermassive black hole see their orbital orientations diffuse efficiently, a process called “vector resonant relaxation”. In particular, stars within the same disc, i.e. neighbors in orientations, will slowly diffuse away from one another through this stochastic process. We use jointly (i) detailed kinetic predictions for the efficiency of this dilution and (ii) the recent observation of a stellar disc around SgrA*, the supermassive black hole at the centre of the Milky-Way, to constrain SgrA*’s unobserved stellar cluster. Notably, we investigate quantitatively the impact of a population of intermediate mass black holes on the survivability of the stellar disc.

Key words: Diffusion - Gravitation - Galaxies: kinematics and dynamics - Galaxies: nuclei

1 INTRODUCTION

Recent outstanding observations keep providing us with new information on the dense cluster orbiting around SgrA*, the supermassive black hole (BH) at the centre of the Milky-Way. These include a thorough census of stellar populations (Ghez et al. 2008; Gillessen et al. 2017) in particular highlighting the presence of a clockwise stellar disc (Levin & Beloborodov 2003; Paumard et al. 2006; Bartko et al. 2009; Lu et al. 2009; Yelda et al. 2014; von Fellenberg et al. 2022), along with the relativistic precession of the star S2 (GRAVITY Collaboration et al. 2020). This wealth of information regarding the dynamical status of SgrA*’s nuclear stellar cluster (Neumayer et al. 2020) is expected to offer new insights on the possible presence of intermediate mass black holes (IMBHs) in these dense regions (see, e.g., Portegies Zwart & McMillan 2002).

The dynamics of stars orbiting a supermassive BH involves an intricate hierarchy of dynamical processes (Rauch & Tremaine 1996; Alexander 2017). In the present work, we focus on the process of vector resonant relaxation (VRR) (Kocsis & Tremaine 2015), i.e. the mechanism through which coherent torques between orbits lead to an efficient diffusion of the stellar orbital orientations. The analytical and numerical studies of VRR have recently seen a surge of new developments to understand in particular (i) the warping of stellar discs (Kocsis & Tremaine 2011); (ii) the enhancement of binary merger rates embedded in galactic nuclei (Hamers et al. 2018); (iii) the non-trivial equilibrium distribution of orientations (Roupas et al. 2017; Takács & Kocsis 2018; Touma et al. 2019; Gruzinov et al. 2020;

Magan et al. 2022; Máthé et al. 2023) possibly leading to formation of discs of IMBHs (Szölgyén & Kocsis 2018); (iv) the rapid (resonant) dynamical friction imposed by a stellar disc onto an IMBH (Ginat et al. 2022; Levin 2022).

Similarly, the potential fluctuations generated by the old background stellar cluster and its putative IMBHs can drive the spontaneous dilution of the presently observed discs of young S-stars. As such, we argue that the present survival of the stellar disc requires that VRR fluctuations are not driven too strongly throughout the disc’s life. In the present work, we build upon Giral Martínez et al. (2020), hereafter G20, and use quantitatively the process of “neighbor separation” by VRR to compare VRR predictions to the observed S-stars. Our aim is to leverage VRR to constrain the stellar content of SgrA*’s cluster, in particular its possible IMBHs.

The paper is organised as follows. In §2, we recall the key elements of VRR. In §3, we detail our inference method. In §4, we apply this method to SgrA* to (loosely) constrain the properties of the likely population of IMBHs orbiting therein. Finally, we conclude in §5. The calculations and numerical details presented in the main text are kept to a minimum and are spread through Appendices.

2 VECTOR RESONANT RELAXATION

We consider a set of $N \gg 1$ stars orbiting around a supermassive BH of mass M_\bullet . We call this background of stars the “bath”. They represent the unobserved populations (old low

arXiv:2305.15998v1 [astro-ph.GA] 25 May 2023

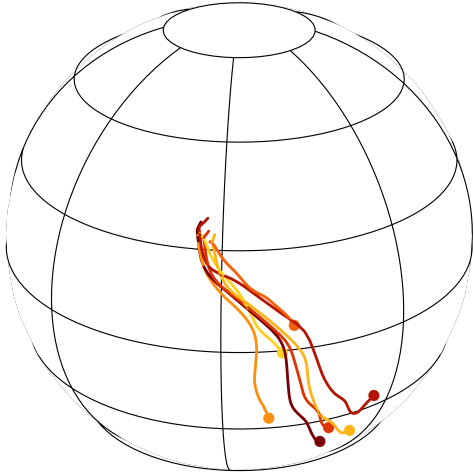


Figure 1. Illustration of the VRR dilution of a disc of 7 stars over 3 Myr when embedded within the Top-Heavy model from §C3. Here, each point represents the instantaneous orbital orientation, $\hat{\mathbf{L}}$, of a star on the unit sphere.

mass stars, IMBHs, etc.). They are responsible for fluctuations in the gravitational potential, and hence drive VRR. Provided that one considers dynamics on timescales longer than the Keplerian motion induced by the central BH (e.g., ~ 16 yr for S2) and the in-plane precession driven by relativistic corrections (e.g., $\sim 3 \times 10^4$ yr for S2), one can orbit-average the dynamics over each star’s mean anomaly and pericentre phase. Stars are formally replaced by massive annuli, see, e.g., fig. 1 in G20. These are characterised by

$$\mathbf{K} = (m, a, e), \quad (1)$$

with m the individual mass, a the semi-major axis, and e the eccentricity. The norm of the angular momentum of a given annulus is $L(\mathbf{K}) = m\sqrt{GM_{\bullet}a(1-e^2)}$ and is conserved during the VRR dynamics. The remaining dynamical quantity is the instantaneous orbital orientation, denoted with the unit vector $\hat{\mathbf{L}}$. We assume that the bath is on average isotropic. Its distribution of orbital parameters is characterised by a distribution function (DF), $n(\mathbf{K})$, normalised to $\int d\mathbf{K} d\hat{\mathbf{L}} n(\mathbf{K}) = N$. Our conventions are spelled out in §A.

In addition to this bath, we consider a population of test stars. These correspond to the observed S-stars forming the clockwise stellar disc. We neglect the mass of these test stars: they only probe the potential fluctuations in the system but do not contribute to it. Ultimately, these stars’ orientations are driven away from one another via VRR, i.e. the disc dissolves as illustrated in Fig. 1. This is the observational signature that we leverage in order to constrain the stellar content of the background bath, i.e. $n(\mathbf{K})$.

Given that the disc stars are massless, investigating the dilution of the disc is formally equivalent to investigating the dilution of pairs of test stars (see §E in G20). Let us consider two disc stars of orbital parameters \mathbf{K}_1 and \mathbf{K}_2 . We assume that at the time of their birth, these stars’ respective angular momentum vectors were separated by some small angle ϕ_0 . As a result of VRR, these two stars are slowly stirred away from one another. This is the process of “neighbor separation” driving the stochastic evolution of $\phi(t)$. This was the process investigated in detail in G20.

In §B, we reproduce and improve upon the main results

of G20. Ultimately, §B provides us with a prediction for the time evolution of the probability distribution function (PDF) of the angular separation

$$t \mapsto P(\phi | t), \quad (2)$$

as a function of time. We emphasise that the statistics of $P(\phi | t)$ depends on (i) the orbital distribution of the background bath, $n(\mathbf{K})$; (ii) the orbital parameters of the two test stars, $(\mathbf{K}_1, \mathbf{K}_2)$; (iii) their initial angular separation, ϕ_0 .

3 INFERENCE METHODS

Since VRR drives a stochastic dynamics, constraints on the properties of SgrA*’s stellar background, i.e. $n(\mathbf{K})$, can only be obtained in a statistical sense. To do so, we use maximum likelihood estimations. We detail our approach in §D and reproduce here only the key assumptions.

Our goal is to constrain the parameters, θ , of SgrA*’s background bath, given some observed angular separations between disc stars. For example, parameters can be the collection $\theta = \{n(\mathbf{K}), \phi_0, T_{\star}\}$, with T_{\star} the ages of the observed stars. For a given pair of test stars (i, j) , we have at our disposal their (conserved) orbital parameters, $\{\mathbf{K}_i, \mathbf{K}_j\}$, along with their current angular separation, ϕ_{ij} . For each θ , we compute the associated predicted PDF, $\phi_{ij} \mapsto P(\phi_{ij} | \theta, \mathbf{K}_i, \mathbf{K}_j)$, according to which ϕ_{ij} could have been drawn. The likelihood of the parameters θ is then proportional to $P(\phi_{ij} | \theta, \mathbf{K}_i, \mathbf{K}_j)$. This is the gist of our method.

To improve upon this approach, we include a few additional effects by (i) marginalising over the dispersion of the predicted log-normal distributions which we use to model the likelihood (§D1); (ii) accounting jointly for all the distinct pairs of test stars of a given disc (§D2); (iii) incorporating measurement errors in the observed S-stars (§D3). In practice, all these effects are included by bootstrapping over independent samples. It is essential to assess the performance of this approach by applying it to tailored numerical simulations of increasing complexity, see §C for details. This is what we now detail.

First, we consider a simple one-population background bath (§C2). In Fig. 2, we report our inferred likelihoods from these fiducial simulations, as one varies respectively (m, γ) , the individual mass and power-law index of the bath, or (ϕ_0, T_{\star}) , the initial angular separation and age of the test stars. The likelihood here corresponds to synthetic observations mimicking our actual analysis of the S-stars around SgrA*. In fact, we display the expectation value of the likelihood over multiple realisations of the observations, in order to provide a stringent test of the model, as detailed in §C2. Although Fig. 2 suffers from a slight bias, our method is able to recover the parameters of the simulated bath. This is reassuring.

We now turn our interest to a astrophysically more relevant astrophysical system, namely the two-population (stars and IMBHs) Top-Heavy model from Generozov & Madigan (2020) (§C3), in which we inject discs of 7 test stars mimicking the observed S-stars. In Fig. 3, we illustrate our expected likelihood as one varies respectively $(m_{\bullet}, \gamma_{\bullet})$ the individual mass and power-index of the IMBH population or (ϕ_0, T_{\star}) the initial angular size of the disc and their (common) stellar

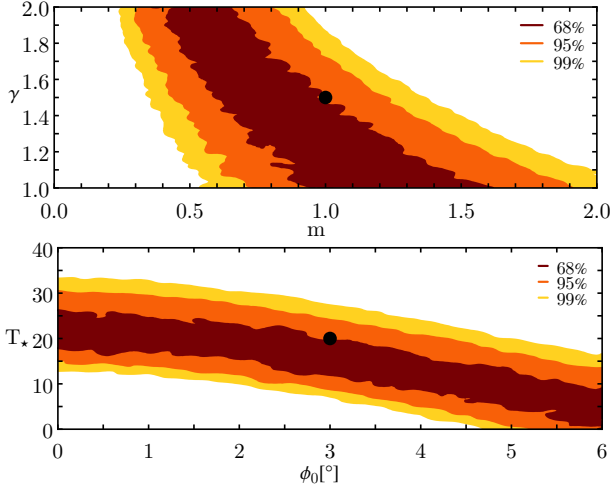


Figure 2. Likelihood for the fiducial one-population simulations (§C2) as one varies (m, γ) (top) or (ϕ_0, T_*) (bottom). The black dot corresponds to the bath effectively simulated and the colored lines to the confidence levels. See §D1 for details.

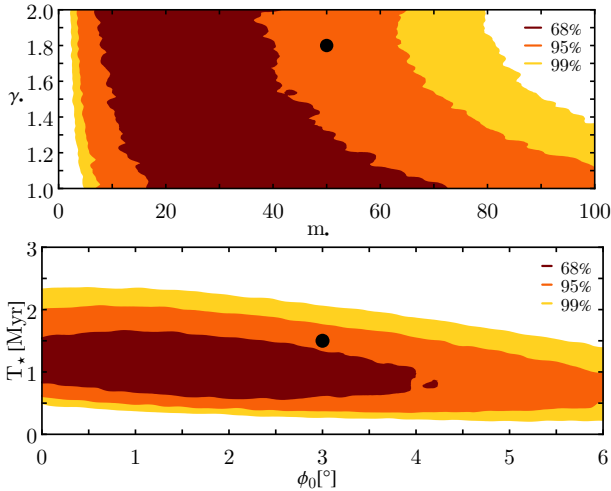


Figure 3. Same as in Fig. 2, but for the two-population simulations from §C3. See §D2 for details.

ages. We average over many realisations of the observations (§D2). We note that the reconstruction is not ideal and suffers from some bias. One should keep these limitations in mind when applying VRR neighbor separation to SgrA*'s clockwise disc.

4 RESULTS FOR SGRA*

We now apply our approach to the clockwise disc of S-stars (see §A). The realm of possible models for SgrA*'s background is extremely large. For the sake of simplicity, we only consider baths similar to the Top-Heavy model from Genozov & Madigan (2020) (§C3). These clusters are therefore characterised by two background populations (stars and IMBHs) each with their own individual mass and power-law index, an initial angular separation for the disc, ϕ_0 (see Eq. C2), and a common stellar age, T_* , for the S-stars. For simplicity, we arbitrarily impose $\phi_0 = 3^\circ$, and fix the age of

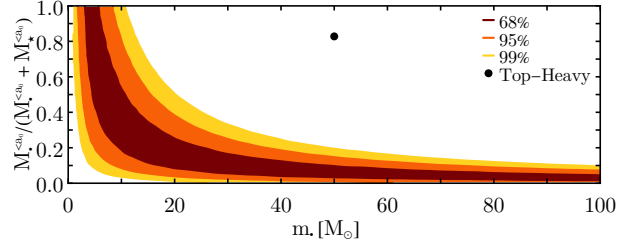


Figure 4. Likelihood estimated from the S-stars' resolved orbits. We assume that SgrA*'s background cluster follows the two-population Top-Heavy model from §C3, and respectively vary $(m_\bullet, M_\bullet(<a_0)/(M_\bullet(<a_0) + M_\star(<a_0)))$ with the total enclosed mass, $M_\bullet(<a_0) + M_\star(<a_0)$, and all the other parameters fixed. The black dot corresponds to the Top-Heavy model (Genozov & Madigan 2020). See §D for details.

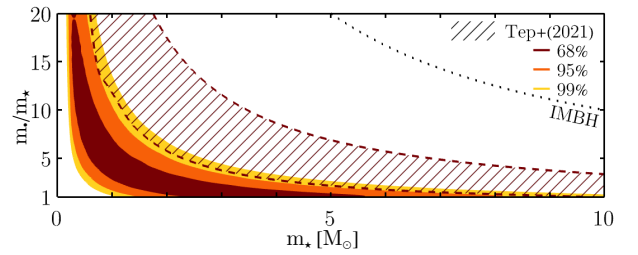


Figure 5. Same as in Fig. 4, this time jointly varying $(m_\star, m_\bullet/m_\star)$ keeping all other parameters fixed. The dashed line corresponds to $m_\bullet = 100M_\odot$ above which the heavy objects are usually considered as IMBHs. The hashed contours correspond to the 68% level lines constrained in Tep et al. (2021) by considering eccentricity relaxation.

the stars to $T_* = 7.1$ Myr (see §A). We marginalise our likelihood over the observational uncertainties in the S-star's orbital parameters from Gillessen et al. (2017), and over the initial orientation of the stellar orbits within a narrow distribution around $\phi_0 = 3^\circ$, following Eq. (C2).

In Fig. 4, we plot this likelihood, varying the individual mass m_\bullet as well as the total IMBH mass fraction $M_\bullet(<a_0)/(M_\bullet(<a_0) + M_\star(<a_0))$, keeping the mass enclosed within a fiducial scale radius a_0 , $M_\bullet(<a_0) + M_\star(<a_0)$, fixed. Interestingly, we find that the Top-Heavy model from Genozov & Madigan (2020) is incompatible with SgrA*'s observed stellar disc. The survival of the disc through the VRR dynamics requires indeed a quieter bath, i.e. a smaller IMBH fraction.

Finally, in Fig. 5, we let the individual masses of the background cluster, m_\star and m_\bullet , vary with the natural constraint $m_\bullet \geq m_\star$, while fixing the total IMBH mass fraction $M_\star(<a_0)$ and $M_\bullet(<a_0)$. In that figure, we find that the survival of SgrA*'s disc requires a drastically smaller individual mass for the background population of heavy particles. Assuming that all the other parameters of the background bath are fixed, the current presence of SgrA*'s disc seems in tension with the presence of IMBHs, as illustrated by the dotted line in that plot.

A similar parameter exploration has recently been presented in the bottom right panel of fig. 3 of Tep et al. (2021). There, the authors used the eccentricity relaxation of the S-stars to constrain SgrA*'s stellar content, assuming that the S-stars were initially born from an initial quasi-circular disc.

In Fig. 5, we reproduce the bottom-right panel of fig. 3 of Tep et al. (2021). It is very interesting to note that both works, although they are using different dynamical processes (scalar vs. vector resonant relaxation) offer similar constraints on SgrA*'s background cluster. They jointly constrain the likelihood of IMBHs orbiting SgrA*. Naturally, one should keep in mind all the limitations of the present exploration, in particular the small number of parameters effectively probed. Future works will focus on exploring larger parameter spaces by sampling from the full likelihood.

5 CONCLUSIONS

We illustrated how a statistical characterisation of VRR used jointly with the recent observation of SgrA*'s clockwise stellar disc allows one to place constraints on the content of SgrA*'s underlying stellar cluster, in particular IMBHs. More precisely, to be compatible with the disc's being still present today, VRR fluctuations cannot be too large, i.e. cannot be too efficient at driving the spontaneous dilution of the disc. Keeping in mind the small range of parameters explored, we showed that the survival of SgrA*'s disc tends to reduce the likelihood for heavy background particles, like IMBHs, to orbit around SgrA*.

Naturally, this paper is only a first step toward fully leveraging VRR to constrain SgrA*'s stellar content: a more thorough exploration of parameter space is a logical next step. We now conclude with a few possible additional venues for future works.

The statistical description of neighbor separation by VRR (§B) relies extensively on the assumption of an isotropic background bath. This is key to simplify the analytical calculations. However, this does not account for any possible anisotropic clustering in orientations, such as IMBHs discs (Szölgvény & Kocsis 2018) and the associated resonant dynamical friction (see, e.g., Szölgvény et al. 2021). Indeed, a rotating background stellar cluster is expected to source (resonant) dynamical friction, possibly leading to an efficient disruption of the disc (Levin 2022). Going beyond isotropy, e.g., axisymmetric distributions, will be the focus of future works.

We also assumed the limit of test particles for the disc stars, i.e. we neglected the self-gravity among them. Contributions from this additional coupling were already investigated numerically in Kocsis & Tremaine (2011), see figs. 6 and 7 therein. It showed that self-gravity increased the coherence of the disc, hence delaying its dilution: the more massive the disc, the longer its survival. Incorporating this additional effect is no easy analytical undertaking.

We neglected the effect of SgrA*'s spin, which via the Lense–Thirring precession (see, e.g., Merritt 2013) can also drive a spontaneous dilution of the disc (Levin & Beloborodov 2003; Fragione & Loeb 2022). We point out that these effects could still be somewhat small here because the disc stars are quite far from SgrA*, $a_{\text{disc}} \gtrsim 50$ mpc. In addition, the appropriate timescale for dilution is the one of phase mixing, i.e. the orbital planes of the disc stars must precess respectively from one another. It would be worthwhile to include this additional effect.

VRR relies on a double orbit-average over both the fast Keplerian motion and the in-plane precession. As a result,

the semi-major axes and eccentricities of each annuli are supposed to be conserved. This amounts to neglecting the possible contributions of scalar resonant relaxation and non-resonant relaxation (Rauch & Tremaine 1996). Although slower, these additional processes could still marginally impact the disc's dilution.

Finally, we expect that future observations, such as ELT (Pott et al. 2018; Davies et al. 2018) and TMT (Do et al. 2019), will soon provide the community with a wealth of resolved orbits around SgrA*, along with their stellar ages. This additional statistics will prove paramount to tighten the present constraints on SgrA*'s stellar content. In particular, the same data will allow one to constrain both the efficiency of eccentricity relaxation (Tep et al. 2021) as well as orientation relaxation (this work). Ultimately, these two dynamical windows should offer complementary constraints on the statistics of the possible IMBHs orbiting around SgrA*.

Data Distribution

The code and the data underlying this article is available through reasonable request to the authors.

ACKNOWLEDGEMENTS

JBF is partially supported by grant Segal ANR-19-CE31-0017 of the French Agence Nationale de la Recherche, and by the Idex Sorbonne Université. AZ was supported by NSF Grants PHY-1912578 and PHY-2207594. JBF warmly thanks F. Leclercq for various suggestions.

APPENDIX A: STELLAR CUSPS IN SGRA*

In this Appendix, we specify our convention for the description of the background bath. Following Gillessen et al. (2017), we fix SgrA*'s mass to $M_{\bullet} = 4.28 \times 10^6 M_{\odot}$. We take SgrA*'s distance from the Earth to be $d = 8.178$ kpc (GRAVITY Collaboration et al. 2019). This is used to obtain the S-stars' semi-major axes from table 3 in Gillessen et al. (2017). Following fig. 12 of Gillessen et al. (2017), we assume that the disc is composed of a total of seven stars, namely (S66, S67, S83, S87, S91, S96, S97). Their ages are inferred from the main-sequence ages measured in table 2 of Habibi et al. (2017), albeit for different S-stars. In practice, we assume that the disc stars' ages are identical and impose $T_{\star} = 7.1$ Myr, the average stellar age of the S-stars with both resolved orbits and constrained main-sequence stellar ages. This large uncertainty on the stars' ages is one the main limitations of the results from the main text.

A given bath is composed of different stellar populations within which all the orbits share the same individual mass. In practice, we make two important assumptions: (i) each population follows a power-law distribution in semi-major axes; (ii) each population follows a thermal distribution in eccentricities. As a consequence, a given population is characterised by three numbers, namely (i) γ , the slope of the power-law profile in semi-major axis; (ii) m , the individual mass of the particles; (iii) $M(< a_0)$, the total mass physically enclosed within a radius a_0 , a radius of reference.

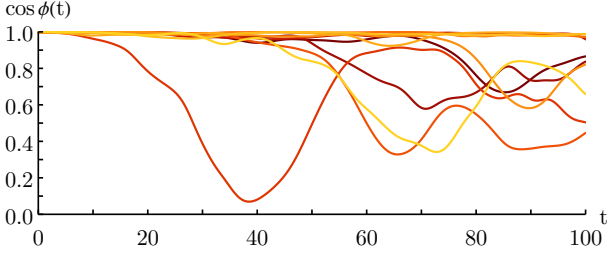


Figure B1. Typical random walks of pairwise angular separations, $\cos \phi(t)$, as observed in the simple setup from §C2.

More precisely, for a given population the number of stars per unit semi-major axis, a , is given by

$$N(a) = (3-\gamma) \frac{N_0}{a_0} \left(\frac{a}{a_0}\right)^{2-\gamma}, \quad (\text{A1})$$

where we introduced $N_0 = g(\gamma) N(<a_0)$ with

$$g(\gamma) = 2^{-\gamma} \sqrt{\pi} \Gamma(1+\gamma) / \Gamma(\gamma - \frac{1}{2}), \quad (\text{A2})$$

with $\Gamma(x)$ the gamma function and $N(<a_0) = M(<a_0)/m$ the number of stars physically enclosed within the radius a_0 . We assume that the distribution of eccentricities is thermal, neglecting effects associated with the SgrA*’s loss cone. Eccentricities follow then the PDF

$$f(e) = 2e, \quad (\text{A3})$$

which satisfies the normalisation $\int de f(e) = 1$. Following the convention from §2, the DF of a given background population is therefore

$$n(\mathbf{K}') = \frac{1}{4\pi} \delta_D(m' - m) N(a') f(e'), \quad (\text{A4})$$

recalling that the background populations are assumed to be isotropic on average.

Assuming that the background populations follow power law distributions greatly simplifies the computation of the coherence time, see §I in Fouvry et al. (2019). In practice, following the notations therein, we pre-computed the dimensionless function $f_{\Gamma^2}(e)$ for $0 \leq \gamma \leq 3$ and $0 \leq e \leq 0.99$, on a 300×100 grid, to be interpolated afterwards. This allows for efficient evaluations of the coherence time of the background bath, $T_c(\mathbf{K})$, as defined in Eq. (B7).

APPENDIX B: VRR NEIGHBOR SEPARATION

We are interested in the stochastic evolution of the angle $\phi(t)$ between two test stars’ orbits of parameters $(\mathbf{K}_1, \mathbf{K}_2)$ embedded within a background bath characterised by $n(\mathbf{K})$. Figure B1 illustrates typical random walks undergone by $\cos \phi(t)$ for the simple bath from §C2.

B1 Analytical prediction

Following G20, the dilution of the two test stars can be described via the moments of the correlation function of the stars’ respective orientations, namely

$$t \mapsto \langle P_{\ell_\alpha}(\cos \phi(t)) \rangle, \quad (\text{B1})$$

with P_{ℓ_α} the Legendre polynomials and $\langle \cdot \rangle$ standing for an ensemble average over realisations of the bath and initial

conditions of the two test stars. Following Eq. (21) of G20, these moments evolve according to¹

$$\langle P_{\ell_\alpha}(\cos \phi(t)) \rangle = D_{\ell_\alpha} C_{\ell_\alpha}^\Omega(t) C_{\ell_\alpha}^D(t). \quad (\text{B2})$$

In Eq. (B2), $D_{\ell_\alpha} = \langle P_{\ell_\alpha}(\cos \phi(0)) \rangle$ describes the statistics of the angular separation at $t=0$. Following Eq. (D9) of G20, the function $C_{\ell_\alpha}^\Omega(t)$ describes the separation driven by the differences in the two particles orbital parameters, i.e. driven by $\mathbf{K}_1 \neq \mathbf{K}_2$. It reads

$$C_{\ell_\alpha}^\Omega(t) = \exp \left[-\frac{1}{2} A_{\ell_\alpha} \sum_{\ell} B_{\ell} I_{\ell}^{-}(\mathbf{K}_1, \mathbf{K}_2, t) \right], \quad (\text{B3})$$

Similarly, following Eq. (D10) of G20², the function $C_{\ell_\alpha}^D(t)$ captures the separation sourced by the differences in the test particles’ initial orientations. It reads

$$C_{\ell_\alpha}^D(t) = \exp \left[-\sum_{\ell, \ell_\gamma} \frac{D_{\ell_\alpha} - D_{\ell_\gamma}}{(2\ell_\alpha + 1) D_{\ell_\alpha}} (E_{\ell_\alpha \ell \ell_\gamma}^L)^2 I_{\ell}^{+}(\mathbf{K}_1, \mathbf{K}_2, t) \right]. \quad (\text{B4})$$

In Eqs. (B3) and (B4), we defined the integrals

$$\begin{aligned} I_{\ell}^{-}(\mathbf{K}_1, \mathbf{K}_2, t) &= \int d\mathbf{K} n(\mathbf{K}) (\mathcal{J}_{\ell}[\mathbf{K}_1, \mathbf{K}] - \mathcal{J}_{\ell}[\mathbf{K}_2, \mathbf{K}])^2 \\ &\quad \times \frac{2T_c^2(\mathbf{K})}{A_{\ell}} \chi[\sqrt{A_{\ell}/2}(t/T_c(\mathbf{K}))], \\ I_{\ell}^{+}(\mathbf{K}_1, \mathbf{K}_2, t) &= \int d\mathbf{K} n(\mathbf{K}) \mathcal{J}_{\ell}[\mathbf{K}_1, \mathbf{K}_2] \mathcal{J}_{\ell}[\mathbf{K}_2, \mathbf{K}] \\ &\quad \times \frac{2T_c^2(\mathbf{K})}{A_{\ell}} \chi[\sqrt{A_{\ell}/2}(t/T_c(\mathbf{K}))]. \end{aligned} \quad (\text{B5})$$

We also introduced the coefficients

$$A_{\ell} = \ell(\ell+1); \quad B_{\ell} = \frac{1}{8\pi} \ell(\ell+1)(2\ell+1), \quad (\text{B6})$$

along with the bath’s coherence time

$$\frac{1}{T_c^2(\mathbf{K})} = \sum_{\ell} B_{\ell} \int d\mathbf{K}' n(\mathbf{K}') \mathcal{J}_{\ell}^2[\mathbf{K}, \mathbf{K}'], \quad (\text{B7})$$

where the coupling coefficients, $\mathcal{J}_{\ell}[\mathbf{K}, \mathbf{K}']$, are given in §A of G20. In practice, these coefficients are pre-computed using the same approach as in Magnan et al. (2022). Equation (B4) also involves the isotropic Elsasser coefficients, $E_{\ell_\alpha \ell \ell_\gamma}^L$, as spelled out in §B of Fouvry et al. (2019). Finally, we introduced the dimensionless function

$$\chi(\tau) = \int_0^{\tau} d\tau_1 \int_0^{\tau} d\tau_2 e^{-(\tau_1 - \tau_2)^2} = e^{-\tau^2} - 1 + \sqrt{\pi} \tau \text{erf}(\tau), \quad (\text{B8})$$

which captures the transition between the ballistic and diffusive regimes (Fouvry et al. 2019).

Unfortunately, as argued in §4 of G20, the analytical prediction from Eq. (B2) does not provide a good match to the late-time behavior of the dilution of test stars that start with very similar initial orientations. To alleviate this difficulty, we follow G20 and rely on a “piecewise” prediction.

B2 Piecewise prediction

Regardless of the initial similarity between the test particles, Eq. (B2) works well on short timescales, i.e. for $t \lesssim T_c(\mathbf{K})$. As such, we give ourselves the timelapse

$$\Delta t = \text{Min}[T_c(\mathbf{K}_1), T_c(\mathbf{K}_2)], \quad (\text{B9})$$

¹ Equation (21) of G20 is missing a $1/(4\pi)$ in its rhs.

² Equation (D10) of G20 is missing a minus sign in its rhs.

and set out to construct the sequence of angular separations

$$\cos \phi_0 \rightarrow \dots \rightarrow \cos \phi_n = \cos \phi(t=n\Delta t). \quad (\text{B10})$$

This prediction is Markovian in the sense that we treat the transition $\cos \phi_i \rightarrow \cos \phi_{i+1}$ as independent of the past history of the test particles.

Following Eq. (G1) of G20, we can write

$$\langle P_\ell(\cos \phi_{i+1}) \rangle = \int d(\cos \phi_i) \rho_i(\cos \phi_i) \langle P_\ell(\cos \phi_{i+1}) | \cos \phi_i \rangle. \quad (\text{B11})$$

In that expression, $\langle P_\ell(\cos \phi_{i+1}) | \cos \phi_i \rangle$ follows from Eq. (B2) evaluated after a time $t=\Delta t$ and assuming that the test particles are initially separated by the fixed angle ϕ_i , i.e. $D_\ell = P_\ell(\cos \phi_i)$. Equation (B11) also involves $\rho_i(\cos \phi_i)$, the PDF of $\cos \phi_i$, which is unknown. Our goal is therefore to average over it.

B3 Perturbative expansion

We now make progress by performing a perturbative expansion of Eq. (B2) for small angles.³ For $\cos \phi_0 \rightarrow 1$, the Legendre polynomials obey the second-order expansion

$$P_\ell(\cos \phi_0) \simeq 1 - \frac{1}{2}A_\ell(1 - \cos \phi_0) + \frac{1}{16}C_\ell(1 - \cos \phi_0)^2, \quad (\text{B12})$$

with $C_\ell = A_\ell(A_\ell - 2)$. Let us now expand Eq. (B4) at second order in $1 - \cos \phi_0$. We write

$$\frac{D_{\ell_\alpha} - D_{\ell_\gamma}}{(2\ell_\alpha + 1)D_{\ell_\alpha}} \simeq \frac{1}{2}(1 - \cos \phi_0) \frac{A_{\ell_\gamma} - A_{\ell_\alpha}}{2\ell_\alpha + 1} \quad (\text{B13})$$

$$+ \frac{1}{16}(1 - \cos \phi_0)^2 \frac{C_{\ell_\alpha} - C_{\ell_\gamma} + 4A_{\ell_\alpha}(A_{\ell_\gamma} - A_{\ell_\alpha})}{2\ell_\alpha + 1},$$

where we used $D_\ell = P_\ell(\cos \phi_0)$. Pursuing the calculation, we can perform the sum over ℓ_γ in Eq. (B4) to get

$$\sum_{\ell_\gamma} \frac{D_{\ell_\alpha} - D_{\ell_\gamma}}{(2\ell_\alpha + 1)D_{\ell_\alpha}} (E_{\ell_\alpha \ell_\gamma}^L)^2 \simeq \frac{1}{2}(1 - \cos \phi_0) A_{\ell_\alpha} B_\ell (A_\ell - 2)$$

$$+ \frac{1}{16}(1 - \cos \phi_0)^2 A_{\ell_\alpha} B_\ell (A_\ell - 2)(A_{\ell_\alpha} - A_\ell + 6). \quad (\text{B14})$$

To get this expression, we used some contraction rules of the isotropic Elsasser coefficients, namely Eqs. (B3) and (B4) in G20, along with

$$\sum_{\ell_\gamma} \frac{1}{2\ell_\alpha + 1} (E_{\ell_\alpha \ell_\gamma}^L)^2 C_{\ell_\gamma} = A_{\ell_\alpha} B_\ell$$

$$\times [12 - 6A_\ell - 6A_{\ell_\alpha} + 3A_\ell A_{\ell_\alpha} + C_\ell + C_{\ell_\alpha}]. \quad (\text{B15})$$

At second-order in $(1 - \cos \phi_0)$, Eq. (B2) becomes

$$\langle P_{\ell_\alpha}(\cos \phi(t)) | \cos \phi_0 \rangle \simeq P_{\ell_\alpha}(\cos \phi_0) C_{\ell_\alpha}^\Omega(t) C_{\ell_\alpha}^D(t), \quad (\text{B16})$$

with

$$C_{\ell_\alpha}^\Omega(t) \simeq \exp\left[-\frac{1}{2}A_{\ell_\alpha} \Psi^-(\mathbf{K}_1, \mathbf{K}_2, t)\right], \quad (\text{B17})$$

and

$$C_{\ell_\alpha}^D(t) \simeq \exp\left[-\frac{1}{2}A_{\ell_\alpha}(1 - \cos \phi_0) \Psi^+(\mathbf{K}_1, \mathbf{K}_2, t)\right] \quad (\text{B18})$$

$$- \frac{1}{16}A_{\ell_\alpha}(1 - \cos \phi_0)^2 (A_{\ell_\alpha} \Psi^+(\mathbf{K}_1, \mathbf{K}_2, t) - \Psi^{++}(\mathbf{K}_1, \mathbf{K}_2, t)).$$

³ Here, we improve upon G20 and perform a second-order expansion. Though, the crux of the calculations remains identical.

In these expressions, we introduced

$$\Psi^-(\mathbf{K}_1, \mathbf{K}_2, t) = \sum_{\ell} B_\ell I_\ell^-(\mathbf{K}_1, \mathbf{K}_2, t), \quad (\text{B19})$$

$$\Psi^+(\mathbf{K}_1, \mathbf{K}_2, t) = \sum_{\ell} B_\ell (A_\ell - 2) I_\ell^+(\mathbf{K}_1, \mathbf{K}_2, t),$$

$$\Psi^{++}(\mathbf{K}_1, \mathbf{K}_2, t) = \sum_{\ell} B_\ell (A_\ell - 2)(A_\ell - 6) I_\ell^+(\mathbf{K}_1, \mathbf{K}_2, t)$$

In practice, the integrals over (a, e) appearing in Eq. (B19) are computed using the standard midpoint rule with $K_a = 100$ nodes sampled uniformly in logarithm in the domain $\text{Max}[a_1, a_2] \times 10^{-3} \leq a \leq \text{Min}[a_1, a_2] \times 10^3$, and using $K_e = 20$ nodes uniformly within the domain in e of the considered system.

B4 Propagating the moments

We continue the calculation by expanding explicitly the rhs of Eq. (B16) at second order in $(1 - \cos \phi_0)$. We have

$$\langle P_{\ell_\alpha}(\cos \phi(t)) | \cos \phi_0 \rangle \simeq a_{\ell_\alpha} + b_{\ell_\alpha} P_1(\cos \phi_0) + c_{\ell_\alpha} P_2(\cos \phi_0). \quad (\text{B20})$$

In that expressions, the coefficients (a_ℓ, b_ℓ, c_ℓ) read

$$a_\ell = u_\ell + \frac{1}{12}A_\ell u_\ell \{v_\ell - 6\Psi^+ - 8\},$$

$$b_\ell = -\frac{1}{8}A_\ell u_\ell \{v_\ell - 4\Psi^+ - 6\},$$

$$c_\ell = \frac{1}{24}A_\ell u_\ell \{v_\ell - 2\}, \quad (\text{B21})$$

where we introduced

$$u_\ell = e^{-\frac{1}{2}A_\ell \Psi^-}; \quad v_\ell = \Psi^{++} + A_\ell(1 + \Psi^+)(1 + 2\Psi^+), \quad (\text{B22})$$

and used the shortened notation $\Psi^- = \Psi^-(\mathbf{K}_1, \mathbf{K}_2, t)$, and similarly for Ψ^+ and Ψ^{++} .

We now have everything at our disposal to predict jointly both moments $\langle P_1(\cos \phi_i) \rangle$ and $\langle P_2(\cos \phi_i) \rangle$. Let us introduce the vector and matrices

$$\mathbf{P}_i = \begin{pmatrix} \langle P_1(\cos \phi_i) \rangle \\ \langle P_2(\cos \phi_i) \rangle \end{pmatrix}; \quad \mathbf{A} = \begin{pmatrix} a_1 \\ a_2 \end{pmatrix}; \quad \mathbf{M} = \begin{pmatrix} b_1 & c_1 \\ b_2 & c_2 \end{pmatrix}, \quad (\text{B23})$$

so that Eq. (B20), evaluated at time $t = \Delta t$, reads

$$\mathbf{P}_{i+1} = \mathbf{A} + \mathbf{M} \mathbf{P}_i. \quad (\text{B24})$$

The fixed point of this iteration is $\mathbf{R} = [\mathbf{I} - \mathbf{M}]^{-1} \mathbf{A}$, and can be used to construct the generic solution

$$\mathbf{P}_i = \mathbf{R} + \mathbf{M}^i [\mathbf{P}_0 - \mathbf{R}]. \quad (\text{B25})$$

To obtain a ‘‘continuous’’ prediction from this discrete solution, we diagonalise \mathbf{M} via $\mathbf{M} = \mathbf{U} \text{Diag}[\lambda_1, \lambda_2] \mathbf{U}^{-1}$, which gives $\mathbf{M}^i = \mathbf{U} \text{Diag}[\lambda_1^i, \lambda_2^i] \mathbf{U}^{-1}$. To obtain a continuous prediction, we finally make the replacement $i \rightarrow t/\Delta t$, assuming that the two eigenvalues (λ_1, λ_2) are either both positive or complex conjugate⁴.

In Fig. B2, we compare the initial time-evolution of the first two moments, $\langle P_1(\cos \phi(t)) \rangle$ and $\langle P_2(\cos \phi(t)) \rangle$, between the present kinetic modelling and fiducial numerical simulations (§C2). While the match is not ideal, we emphasize that the prediction still succeeds at predicting the slow

⁴ This is not guaranteed a priori by the present expansion. In practice, for all the background bath and pairs of test particles considered, this was, fortunately, always the case.

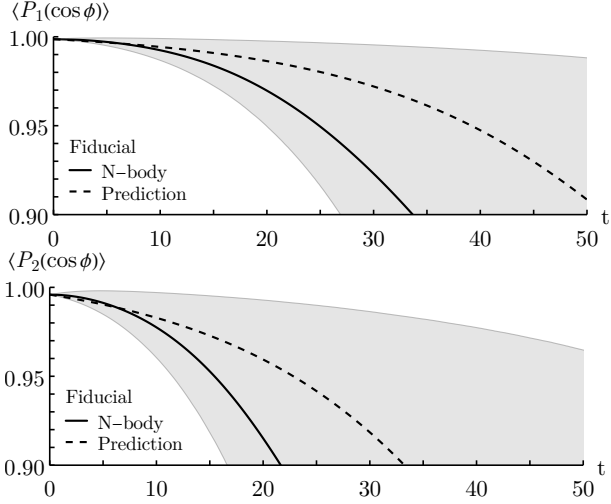


Figure B2. Time evolution of the two first moments $\langle P_1(\cos \phi) \rangle$ (top) and $\langle P_2(\cos \phi) \rangle$ (bottom) for the fiducial bath from §C2. The solid line is measured in numerical simulations, with the gray region highlighting the 16% and 84% levels among the available realisations. The dashed line is the piecewise prediction from §B4.

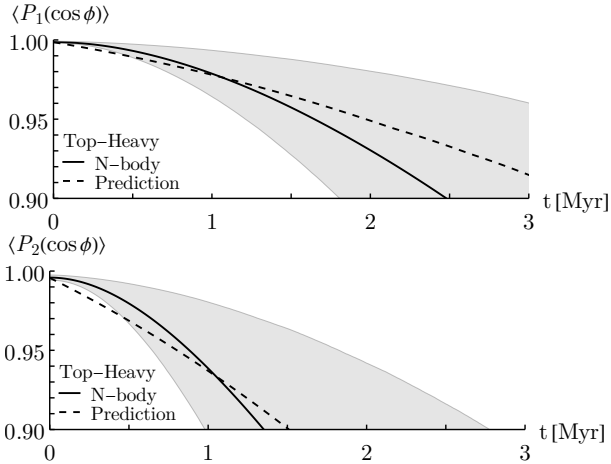


Figure B3. Same as in Fig. B2, but for the two-population bath from §C3. Here, $\langle P_\ell(\cos \phi) \rangle$ is averaged over all the pairs of stars in discs composed of 7 stars each. See the text for details.

initial onset of separation, i.e. the plateau that the naive application of the analytical formula from Eq. (B2) cannot recover.

In Fig. B3, we illustrate the same measurement for the more realistic Top-Heavy model (§C3). In that case, every disc is composed of 7 stars and sustains therefore 21 independent pairs of stars. In Fig. (B3), $\langle P_\ell(\cos \phi) \rangle$ stands therefore for the average over all these pairs of stars. To compute the kinetic prediction, following Eq. (C2), we drew 100 independent initial conditions for 100 discs, following Eq. (C2). These are then used as initial conditions to compute the prediction from §B4. Finally, we average the Legendre moments over this large sample of pairs. Reassuringly, Figs. B2 and B3 exhibit similar trends.

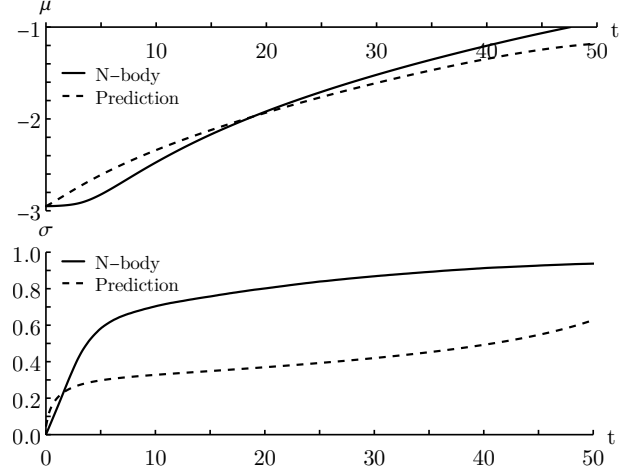


Figure B4. Time evolution of the log-normal parameters μ (top) and σ (bottom) for the fiducial simulations from §C2. The solid line is fitted from the numerical simulations, while the dashed line is the prediction from §B5.

B5 Log-normal ansatz

We now have at our disposal a description for the initial time-evolution of the first two moments $\langle P_1(\cos \phi(t)) \rangle$ and $\langle P_2(\cos \phi(t)) \rangle$. Inspired by §II in G20, we now impose the ansatz that the random variable $\phi(t)$ follows a log-normal PDF at all time. This is a strong assumption. The PDF reads

$$P(\phi | \mu, \sigma) = \frac{1}{\phi \sigma \sqrt{2\pi}} \exp\left[-(\ln \phi - \mu)^2 / (2\sigma^2)\right], \quad (\text{B26})$$

for some parameters μ, σ .

Unfortunately, our predictions for $(\langle P_1 \rangle, \langle P_2 \rangle)$ are not guaranteed to be realisable, i.e. there might not exist a well-defined positive PDF complying with these provided moments. Therefore, to estimate (μ, σ) from $(\langle P_1 \rangle, \langle P_2 \rangle)$, we proceed by minimising the distance $d = (\langle P_1 \rangle - P_1[\mu, \sigma])^2 + (\langle P_2 \rangle - P_2[\mu, \sigma])^2$ over (μ, σ) . In that expression, the moments $P_\ell[\mu, \sigma]$ are efficiently approximated following eq. (1.3) of Asmussen et al. (2016). More precisely, we use

$$\begin{aligned} \langle \cos(\ell \phi) \rangle &= \text{Re} \left[\int_0^{+\infty} d\phi e^{i\ell \phi} P(\phi | \mu, \sigma) \right] \\ &\simeq \text{Re} \left[e^{-w(2+w)/(2\sigma^2)} / \sqrt{1+w} \right], \end{aligned} \quad (\text{B27})$$

with $w = W[-i\ell\sigma^2 e^\mu]$, $W[z]$ the Lambert function, and the Legendre moments naturally follow. This same expression can also be used to compute the gradients $\partial P_\ell[\mu, \sigma] / \partial(\mu, \sigma)$, which are used by the optimiser. In practice, the optimisation is performed using the LBFGS algorithm from `Optim.jl` (Mogensen & Riseth 2018).

In Fig. B4, we compare the time-evolution of the two lognormal parameters, (μ, σ) , as obtained from the kinetic prediction and directly fitted from the numerical simulations. The match for μ is quite good, while the VRR formalism somewhat fails at predicting σ .

Finally, in Fig. B5, we illustrate the PDF of the angles ϕ at various times, and compare it with the predicted log-normal ansatz. In that figure, we note that using the predicted μ and fitting σ from the PDF offers a very sat-

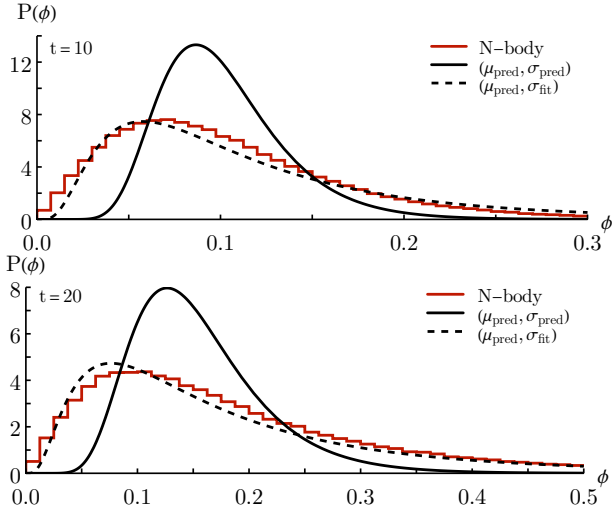


Figure B5. Illustration of the PDF of the angle $\phi(t)$ in the fiducial simulations from §C2 for $t=10$ (top) and $t=20$ (bottom). The full lines correspond to the prediction using both (μ, σ) predicted in §B5, while the dashed lines only use the predicted μ and subsequently fit σ from the empirical histograms.

isfactory match. This motivates the marginalisation over σ when performing likelihood estimations (§D1).

B6 Stitching

Unfortunately, because it relies on a perturbative expansion for small angles (§B3), the piecewise prediction from Eq. (B25) cannot be used for arbitrarily large angular separation, see, e.g., fig. 6 in G20. To circumvent this issue, we use Eq. (B25) only if the following conditions are all met: (i) $\langle \cos \phi \rangle \geq \langle \cos \phi_{\text{cut}} \rangle = 0.8$, i.e. the two test particles are close neighbors; (ii) both $\partial \langle P_1(\cos \phi(t)) \rangle / \partial t$ and $\partial \langle P_2(\cos \phi(t)) \rangle / \partial t$ are negative, i.e. the correlations decay. In any other situations, we revert back to the straightforward application of the analytical result from Eq. (B2). We now detail how this “stitching” between the piecewise and analytical predictions can be made in practice.

Equation (B3) is straightforward to evaluate for $\ell_\alpha = 1, 2$. To evaluate Eq. (B4), we first estimate the values of $D_\ell = \langle P_\ell(\cos \phi) \rangle$ using Eq. (B27). We then use the exclusion rules of the isotropic Elsasser coefficients, $E_{\ell_\alpha \ell_\gamma}^L$, see Eq. (B2) in G20, to perform the sum over ℓ_γ in Eq. (B4). More precisely, for the particular cases $\ell_\alpha = 1$ (resp. $\ell_\alpha = 2$), the range of this sum reduces to $\ell_\gamma = \ell$ (resp. $\ell_\gamma = \ell - 1, \ell + 1$). We also rely on the simple relations

$$\begin{aligned} (E_{1\ell\ell}^L)^2 &= 6B_\ell, \\ (E_{2,\ell,\ell-1}^L)^2 &= 15B_\ell - \frac{45}{8\pi} A_\ell, \\ (E_{2,\ell,\ell+1}^L)^2 &= 15B_\ell + \frac{45}{8\pi} A_\ell. \end{aligned} \quad (\text{B28})$$

We ultimately obtain the explicit expressions

$$\begin{aligned} C_1^{\text{D}}(t) &= \exp \left[- \sum_{\ell} B_\ell \frac{2(D_1 - D_\ell)}{D_1} I_\ell^+(\mathbf{K}_1, \mathbf{K}_2, t) \right], \\ C_2^{\text{D}}(t) &= \exp \left[- \sum_{\ell} \frac{6B_\ell}{D_2} (D_2 - D_{\ell-1} \frac{\ell-1}{2\ell+1} - D_{\ell+1} \frac{\ell+2}{2\ell+1}) \right], \end{aligned}$$

$$\times I_\ell^+(\mathbf{K}_1, \mathbf{K}_2, t) \Big], \quad (\text{B29})$$

to stitch the piecewise and analytical predictions.

Following all these manipulations, for a given background bath, $n(\mathbf{K})$, a given pair of test particles, $(\mathbf{K}_1, \mathbf{K}_2)$, and a given initial angular separation, ϕ_0 , we have at our disposal a prediction for the time evolution of the PDF of the angular separation, $t \mapsto P(\phi|t)$. It is this PDF that is used in the likelihood estimations.

APPENDIX C: NUMERICAL SIMULATIONS

In order to assess the validity of our approach, it is important to test it on numerical simulations of background baths of increasing complexity.

C1 Numerical simulations

The numerical simulations were performed using a multipole algorithm similar to the one presented in Fouvy et al. (2022), here adapted to the simpler case of VRR. Here, we only outline the main elements of the algorithm.

All the radial orbit averages appearing in the coupling coefficients \mathcal{J}_ℓ are replaced by discrete sampling with K nodes in eccentric anomaly. The interaction Hamiltonian is truncated to the maximum harmonic ℓ_{max} . Inspired by Fouvy et al. (2022), the rates of change, $d\hat{\mathbf{L}}/dt$, are computed in $\mathcal{O}(NK\ell_{\text{max}}^2)$ operations owing to prefix sums. We rewrite the equations of motion as precession equations of the form $d\hat{\mathbf{L}}/dt = \boldsymbol{\Omega} \times \hat{\mathbf{L}}$. The dynamics is integrated using the structure-preserving MK2 scheme (see Fouvy et al. 2022) with a constant timestep h . This ensures the exact conservation of $|\hat{\mathbf{L}}| = 1$ throughout the evolution.

C2 One-population bath

Similarly to §F of G20, we consider a single-population background bath. Fixing the units to $G = M_\bullet = 1$, we assume that it is composed of $N = 10^3$ stars of individual mass $m = 1$. Their distribution in a is proportional to $a^{2-\gamma}$ with $\gamma = 1.5$, and limited to $1 \leq a \leq 100$. Finally, their distribution in eccentricities is proportional to e and limited to $0 \leq e \leq 0.3$.

For the test stars, we consider pairs of independent test particles with $(a_1, e_1) = (9.5, 0.15)$ and $(a_2, e_2) = (10.5, 0.05)$. For each realisation, we inject 500 pairs of test particles with an initial angular separation set by $\phi_0 = 3.0^\circ$. We performed a total of 500 realisations. Following §C1, we used $K = 20$, $\ell_{\text{max}} = 10$, $h = 10^{-3}$, and integrated up to $t_{\text{max}} = 100$. Each realisation required ~ 0.5 h of computation on two cores, with final relative errors in the total energy (resp. total angular momentum) of order 10^{-10} (resp. 10^{-10}).

C3 Two-population bath

We consider a more involved bath better mimicking SgrA*. This is the Top-Heavy model from Generozov & Madigan (2020), also reproduced in eq. (14) of Tep et al. (2021). We consider the same BH mass as in §A. The bath is composed of two populations, namely stars and IMBHs, with

$$[\gamma_*, m_*, M_* (< a_0)] = [1.5, 1 M_\odot, 7.9 \times 10^3 M_\odot],$$

$$[\gamma_\bullet, m_\bullet, M_\bullet(<a_0)] = [1.8, 50 M_\odot, 38 \times 10^3 M_\odot], \quad (\text{C1})$$

fixing the scale radius to $a_0 = 100$ mpc. The distribution of eccentricities for both populations is proportional to e and limited to the range $0 \leq e \leq 0.99$.

In practice, we can only simulate a finite number of background particles, hence a finite range in semi-major axes. The minimum (resp. maximum) semi-major axis of the disc stars is $a_{\min}^* \simeq 45$ mpc (resp. $a_{\max}^* \simeq 109$ mpc) as given by S67 (resp. S87). We fix the range of semi-major axes for the bath populations to $a_{\min} \leq a \leq a_{\max}$ with $a_{\min} = a_{\min}^*/\eta$, $a_{\max} = a_{\max}^*\eta$, and $\eta = 5$. The number of background stars is then $N_\star = \int_{a_{\min}}^{a_{\max}} da N(a)$, with $N(a)$ following Eq. (A1). In practice, we find $N_\star = 83\,136$ and $N_\bullet = 5\,466$.

In each realisation, we inject a total of 100 independent discs composed of 7 test stars with orbital parameters following §A. The disc stars' orientations are drawn from a Von Mises-Fischer PDF (see §C2 in G20)

$$P(\hat{\mathbf{L}}) \propto e^{\kappa \hat{\mathbf{L}}_0 \cdot \hat{\mathbf{L}}} \quad (\text{C2})$$

of concentration $\kappa = 2/(1 - \cos \phi_0)$ with $\phi_0 = 3^\circ$, and $\hat{\mathbf{L}}_0$ the disc's mean orientation drawn uniformly on the unit sphere. We performed a total of 500 realisations using $K = 20$, $\ell_{\max} = 10$, $h = 0.4$ kyr, and integrated up to $t_{\max} = 10$ Myr. Each realisation required ~ 36 h of computation on two cores, with final relative errors in the total energy (resp. total angular momentum) of order 10^{-7} (resp. 10^{-8}).

APPENDIX D: LIKELIHOOD ESTIMATION

Ultimately, our goal is to constrain some parameters, θ , for the background bath. Let us first assume that we have at our disposal one observed angular separation, ϕ_{ij} , between two test stars. We can write the likelihood of this angular separation given the bath parameters θ and the conserved orbital parameters $(\mathbf{K}_i, \mathbf{K}_j)$ as

$$P(\phi_{ij} | \theta, \mathbf{K}_i, \mathbf{K}_j) = A \int d\mu d\sigma P(\phi_{ij} | \mu, \sigma) P(\mu, \sigma | \theta, \mathbf{K}_i, \mathbf{K}_j), \quad (\text{D1})$$

with A a normalisation constant and $P(\phi | \mu, \sigma)$ the log-normal PDF from Eq. (B26). In addition, we also introduced

$$P(\mu, \sigma | \theta) = \delta_{\text{D}}[\mu - \tilde{\mu}(\theta, \mathbf{K}_i, \mathbf{K}_j)] \delta_{\text{D}}[\sigma - \tilde{\sigma}(\theta, \mathbf{K}_i, \mathbf{K}_j)], \quad (\text{D2})$$

with δ_{D} the Dirac delta, and $(\tilde{\mu}(\theta, \mathbf{K}_i, \mathbf{K}_j), \tilde{\sigma}(\theta, \mathbf{K}_i, \mathbf{K}_j))$ the kinetic predictions of the log-normal parameters for some given bath, as detailed in §B5. The likelihood $P(\phi_{ij} | \theta, \mathbf{K}_i, \mathbf{K}_j)$ is directly proportional to the posterior probability $P(\theta | \phi_{ij}, \mathbf{K}_i, \mathbf{K}_j)$ derived from the measured parameters $(\phi_{ij}, \mathbf{K}_i, \mathbf{K}_j)$, provided we assume flat priors. In this study, we use the likelihood as a proxy for the posterior measurements of the bath's parameters.

D1 Marginalising over σ

In Fig. B4, we noted that our prediction for $\tilde{\sigma}(\theta, \mathbf{K}_i, \mathbf{K}_j)$ is poor. As a consequence, we marginalise over σ . We write

$$P(\mu, \sigma | \theta, \mathbf{K}_i, \mathbf{K}_j) = P(\sigma | \mu) P(\mu | \theta, \mathbf{K}_i, \mathbf{K}_j), \quad (\text{D3})$$

with $P(\mu | \theta, \mathbf{K}_i, \mathbf{K}_j) = \delta_{\text{D}}[\mu - \tilde{\mu}(\theta, \mathbf{K}_i, \mathbf{K}_j)]$ and assuming a flat prior for σ , namely

$$P(\sigma | \mu) = \mathbf{1}_{0 \leq \sigma \leq 1}, \quad (\text{D4})$$

with $\mathbf{1}$ the indicator function inspired by the range in σ effectively observed in Fig. B4. Injecting Eq. (D3) into Eq. (D1), we can perform the integral over $d\mu d\sigma$ to get

$$P(\phi_{ij} | \theta, \mathbf{K}_i, \mathbf{K}_j) = A I(\phi_{ij} | \tilde{\mu}(\theta, \mathbf{K}_i, \mathbf{K}_j)), \quad (\text{D5})$$

where we introduced

$$I(\phi | \mu) = \int d\sigma P(\phi | \mu, \sigma) P(\sigma | \mu) = \frac{\Gamma[0, \frac{1}{2}(\ln \phi - \mu)^2]}{2\phi \sqrt{2\pi}}, \quad (\text{D6})$$

with $\Gamma[0, x]$ the incomplete gamma function. If one has a sample $\{\phi_a\}_{1 \leq a \leq n}$ of distinct pairs of stars at one's disposal, with the corresponding $(\mathbf{K}_i, \mathbf{K}_j)$ implicit, Eq. (D5) becomes

$$P(\{\phi_a\} | \theta) = \prod_{a=1}^n A I(\phi_a | \tilde{\mu}(\theta)), \quad (\text{D7})$$

i.e. pairs are treated as independent from one another, and we marginalise over σ for each. The larger $P(\{\phi_a\} | \theta)$, the more likely the data for the given parameters.

We apply this method to the fiducial simulations from §C2, considered at time $T_\star = 20$. To obtain the likelihoods presented in Fig. 2, we fix the bath's parameters to their fiducial values (§C2) except for (m, γ) or (ϕ_0, T_\star) , which we respectively try to infer in the two panels of Fig. 2. To mimick the observed data, for some given parameters, we pick, at random, a total of 21 independent pairs of simulated test stars whose angular separations, $\{\phi_a\}$, are used in Eq. (D7). For every set of parameters, we repeat this procedure 100 times and subsequently average the likelihood over this sample. This has the effect of taking the expectation value of the likelihood over an ensemble of realisations of the observations, and reduces the variation due to the stochastic evolution of the pairs. In that figure, the data was computed on a 500×500 grid of parameters, and subsequently smoothed with a Gaussian filter of standard deviation 6. Finally, a contour labeled $x\%$ corresponds to the level line $P(\theta) = p$ where p follows from $G(p)/G(p=0) = x\%$ with $G(p) = \int_{P(\theta) \geq p} d\theta P(\theta)$.

D2 Dilution of a disc

In practice, we are interested in the dilution of a disc composed of 7 stars of individual orientations $\{\hat{\mathbf{L}}_i\}_{1 \leq i \leq 7}$. From these, we can construct $n = 21$ different pairs of distinct stars of respective angular separations

$$\{\phi_a\}_{1 \leq a \leq n} = \{\cos^{-1}(\hat{\mathbf{L}}_i \cdot \hat{\mathbf{L}}_j)\}_{1 \leq i < j \leq 7}. \quad (\text{D8})$$

We use this sample of separations in Eq. (D7).

Let us now apply our likelihood estimation to the simulations from §C3, which we consider at time $T_\star = 1.5$ Myr. For the likelihoods shown in Fig. 3, we fix the bath's parameters to their fiducial values (§C3) except for $(m_\bullet, \gamma_\bullet)$ or (ϕ_0, T_\star) (with $\kappa = 2/[1 - \cos \phi_0]$), which we respectively try to infer. For a given set of parameters, we pick, at random, one simulated disc. The initial conditions used in the prediction from §B are obtained by drawing 7 stars according to Eq. (C2) and following Eq. (D8) to get the pairs' initial separation. For every parameters, we repeat the procedure 100 times and average $P(\{\phi_a\} | \theta)$ for every pair over this sample, again giving us the expected likelihood function for this synthetic observation. The associated inferences are illustrated in Fig. 3, using the same grid size and smoothing approach as in §D1.

D3 Incorporating measurement errors

When applying the present method to the observed S-stars, we must also account for the measurement errors in the stars' orbital parameters. Fortunately, table 3 of Gillessen et al. (2017) provides us with measurement errors for the stars' semi-major axes, eccentricities, inclinations and longitudes of the ascending nodes. For simplicity, we assume that (i) these errors are independent from one another; (ii) to accommodate the physical ranges of each variables, we assume that the semi-major axes follow Gamma distributions, the eccentricities Beta distributions, and the inclinations and longitudes Gaussian distributions, with the reported means and variances. For a given realisation, the ‘‘observed’’ parameters $\{\mathbf{K}_i, \hat{\mathbf{L}}_i\}_{1 \leq i \leq 7}$ are drawn from these distributions, and used in the likelihood estimation. For each set of parameters, we repeat the procedure 100 times, and average the likelihood over this sample. This has the effect of marginalising the likelihood over the measurements uncertainties, unlike the previous averaging procedures which produce the expectation value of the likelihood for the simulated baths. For SgrA* we have only a single realisation of the dynamics of the S-stars, and this is a major source of the uncertainty in our inferences: this can only be reduced by the inclusion of additional observed stars.

For the inferences presented in §4, we systematically fix $(\gamma_*, \gamma_\bullet) = (1.5, 1.8)$ (see §C3), as well as the age of the disc, $T_* = 7.1$ Myr, and the initial angular size of the disc set by $\phi_0 = 3^\circ$. In Fig. 4, we also fix $m_* = 1 M_\odot$ and the sum $M_*(< a_0) + M_\bullet(< a_0) = 45.9 \times 10^3 M_\odot$ for $a_0 = 100$ mpc, while varying m_\bullet and the mass fraction of IMBHs. For Fig. 5, we fix $[M_*(< a_0), M_\bullet(< a_0)] = [7.9 \times 10^3 M_\odot, 38 \times 10^3 M_\odot]$ and vary m_* and m_\bullet/m_* . Finally, we use the same grid size and smoothing procedure as in §D1.

REFERENCES

Alexander T., 2017, *ARA&A*, 55, 17
 Asmussen S., Jensen J. L., Rojas-Nandayapa L., 2016, *Methodol. Comput. Appl. Probab.*, 18, 441
 Bartko H., et al., 2009, *ApJ*, 697, 1741
 Davies R., et al., 2018, in *Ground-based and Airborne Instrumentation for Astronomy VII*. p. 107021S
 Do T., et al., 2019, *BAAS*, 51, 530
 Fouvry J.-B., Bar-Or B., Chavanis P.-H., 2019, *ApJ*, 883, 161
 Fouvry J.-B., Dehnen W., Tremaine S., Bar-Or B., 2022, *ApJ*, 931, 8
 Fragione G., Loeb A., 2022, *ApJ*, 932, L17
 GRAVITY Collaboration et al., 2019, *A&A*, 625, L10
 GRAVITY Collaboration et al., 2020, *A&A*, 636, L5
 Generozov A., Madigan A.-M., 2020, *ApJ*, 896, 137
 Ghez A. M., et al., 2008, *ApJ*, 689, 1044
 Gillessen S., et al., 2017, *ApJ*, 837, 30
 Ginat Y. B., Panamarev T., Kocsis B., Perets H. B., 2022, *arXiv*, 2211.14784
 Giral Martínez J., Fouvry J.-B., Pichon C., 2020, *MNRAS*, 499, 2714
 Gruzinov A., Levin Y., Zhu J., 2020, *ApJ*, 905, 11
 Habibi M., et al., 2017, *ApJ*, 847, 120
 Hamers A. S., Bar-Or B., Petrovich C., Antonini F., 2018, *ApJ*, 865, 2
 Kocsis B., Tremaine S., 2011, *MNRAS*, 412, 187
 Kocsis B., Tremaine S., 2015, *MNRAS*, 448, 3265
 Levin Y., 2022, *arXiv*, 2211.12754

Levin Y., Beloborodov A. M., 2003, *ApJ*, 590, L33
 Lu J. R., Ghez A. M., Hornstein S. D., Morris M. R., Becklin E. E., Matthews K., 2009, *ApJ*, 690, 1463
 Magnan N., Fouvry J.-B., Pichon C., Chavanis P.-H., 2022, *MNRAS*, 514, 3452
 Máthé G., Szölgvény Á., Kocsis B., 2023, *MNRAS*, 520, 2204
 Merritt D., 2013, *Dynamics and Evolution of Galactic Nuclei*. Princeton University Press
 Mogensen P. K., Riseth A. N., 2018, *J. Open Source Softw.*, 3, 615
 Neumayer N., Seth A., Böker T., 2020, *A&ARv*, 28, 4
 Paumard T., et al., 2006, *ApJ*, 643, 1011
 Portegies Zwart S. F., McMillan S. L. W., 2002, *ApJ*, 576, 899
 Pott J. U., et al., 2018, in *Ground-based and Airborne Instrumentation for Astronomy VII*. p. 1070290
 Rauch K. P., Tremaine S., 1996, *New Astron.*, 1, 149
 Roupas Z., Kocsis B., Tremaine S., 2017, *ApJ*, 842, 90
 Szölgvény Á., Kocsis B., 2018, *Phys. Rev. Lett.*, 121, 101101
 Szölgvény Á., Máthé G., Kocsis B., 2021, *ApJ*, 919, 140
 Takács Á., Kocsis B., 2018, *ApJ*, 856, 113
 Tep K., Fouvry J.-B., Pichon C., Heifsel G., Paumard T., Perrin G., Vincent F., 2021, *MNRAS*, 506, 4289
 Touma J., Tremaine S., Kazandjian M., 2019, *Phys. Rev. Lett.*, 123, 021103
 Yelda S., Ghez A. M., Lu J. R., Do T., Meyer L., Morris M. R., Matthews K., 2014, *ApJ*, 783, 131
 von Fellenberg S. D., et al., 2022, *ApJ*, 932, L6